Observation from Earth of an atypical cloud system in the upper Martian atmosphere[*]

J. Lilensten[1], J. L. Dauvergne[2], C. Pellier[3], M. Delcroix[3], E. Beaudoin[4], M. Vincendon[5], E. Kraaikamp[6], G. Bertrand[3], C. Foster[7], C. Go[8], E. Kardasis[9], A. Pace[10], D. Peach[11], A. Wesley[12], E. Samara[6,13], S. Poedts[13,15], and F. Colas[14]

[1] Univ. Grenoble-Alpes, CNRS, IPAG, 38000 Grenoble, France
    e-mail: jean.lilensten@univ-grenoble-alpes.fr
[2] Société de Planétologie des Pyrénées (S2P), 5 rue Gazan, 75014 Paris, France
[3] Commission des Observations planétaires, Société Astronomique de France, 3 rue Beethoven, 75016 Paris, France
    e-mail: chrispellier@sfr.fr
[4] Université Paris-Saclay, LPS (UMR8502), 510 rue André Rivière, 91400 Orsay, France
    e-mail: emmanuel.beaudoin@universite-paris-saclay.fr
[5] Institut d'Astrophysique Spatiale, Université Paris-Saclay, Orsay, France
[6] Royal Observatory of Belgium, Avenue Circulaire 3, 1180 Brussels, Belgium
[7] Astronomical Society of Southern Africa, Centurion, South Africa
[8] University of San Carlos - Physics Department, Nasipit, Talamban, Cebu City, Philippines
[9] Hellenic Amateur Astronomy Association, Alopekis 42, 10676 Athens, Greece
[10] Canopus Observatory, Ir-Rabat, Malta
[11] British Astronomical Association, Burlington House, Piccadilly, London W1J 0DU, UK
[12] Astronomical Society of Australia, PO Box 145 Rubyvale QLD 4702, Australia
[13] Dept. Mathematics/Centre for mathematical Plasma Astrophysics Celestijnenlaan 200B, 3001 Leuven, Belgium
[14] IMCCE, Observatoire de Paris, PSL Research University, CNRS UMR 8028, Sorbonne Université, 77 avenue Denfert-Rochereau, 75014 Paris, France
[15] Institute of Physics, University of Maria Curie- Pl. M. Curie-Sklodowska 5, 20-031 Lublin, Poland

ABSTRACT

Context. The atmosphere of Mars is characterised by a complex seasonal cycle of cloud formation related to the condensation of CO_2 and H_2O, and to the lifting of surface dust. Several decades of spacecraft observations have provided an impressive amount of data to constrain cloud properties. However, observations of a given cloud obtained from Mars orbit are typically limited in time sampling and spatial coverage. As a complement to this existing dataset, Earth-based telescopic observations have the potential to provide a global and dynamic view of some large-scale Mars clouds.
Aims. On 17 November 2020, Mars and Earth were close to opposition. We took advantage of this configuration to attempt observing large-scale high-altitude atmospheric phenomena from Earth with a high time sampling, over several hours.
Methods. Ten amateur astronomers were coordinated along with professional astronomers to observe Mars.
Results. We observed the occurrence of a large-scale high-altitude cloud system, extending over thousands of kilometres from the equator to 50°S. Over 3 h, it emerged from the night side at 92^{+30}_{-16} km and dissipated on the dayside. It occurred at a solar longitude of 316° (southern summer) concomitantly to a regional dust storm and west of the magnetic anomaly. Despite its high altitude, it was composed of relatively large particles (effective radius in the 1–2 μm range). While dust appears an unlikely candidate, possible composition by CO_2 or H_2O are both conceivable, although the whole properties of the cloud makes it atypical compared to previously reported clouds. We discuss the possible connections with the dust storm, along with the hypothetical role of nucleation from cosmic particle precipitation.
Conclusions. We continuously followed a high-altitude huge cloud system on Mars from Earth, emerging from the Martian night, from its appearance at the terminator until its complete dissipation. It is either a large-grained water ice cloud system or an extended mid-summer dawn CO_2 cloud system.

Key words. planets and satellites: atmospheres – planets and satellites: terrestrial planets

1. Introduction

Exploring Mars has been (and still is) a long-term challenge for humanity. It is beyond of the scope of the current paper to

discuss the full history of this exploration. Ground-based observations from the Earth have been extensive, but exploration by spacecraft have constituted most of today's discoveries since the first successful flyby of Mars on 14–15 July 1965 by NASA's Mariner 4 (Branigan 1965). Today, three operational rovers operate on the surface of Mars: NASA's Curiosity (Kerr 2012) and Perseverance (Stack et al. 2020) rovers, and the CNSA Zhurong

---

[*] Movies associated to Fig. 9 are only available at https://www.aanda.org

rover. Eight orbiters are currently operational: Mars Odyssey (Saunders et al. 2004), Mars Express (Schmidt 2003), Mars Reconnaissance Orbiter (Zurek & Smrekar 2007), Mars Orbiter Mission (Srivastava et al. 2015 and references herein), MAVEN (Leblanc et al. 2018 and references herein), the Trace Gas Orbiter (Metcalfe et al. 2018), the Tianwen-1 orbiter (Liu et al. 2020), and the Hope Mars Mission. The harvest of results from this fleet may lead to underestimating the possibilities offered by observations from the surface of the Earth, but such observations have already revealed their potential for cloud characterisation (Parker et al. 1999; Erard 2000; Bell et al. 2001; Sánchez-Lavega et al. 2015). Mars clouds can indeed be difficult to observe at a global scale from a Mars orbit, due to the limited field of view of these observations whose primary objective is high spatial sampling. Some spacecraft instruments are dedicated to the monitoring of Mars at a global scale and at low resolution (e.g. VMC on board Mars Express, see Hernandez-Bernal et al. 2021a). However, it is difficult to follow the dynamics of a given cloud using a dataset obtained from a spacecraft moving along its orbit. On the other hand, observing Mars from Earth could allow cloud formation and dissipation to be followed over several hours with a broad field of view. On 17 November 2020, Mars and Earth were close to each other with a relative distance of 0.55 AU. Mars solar longitude was 316°. This allowed the upper atmosphere of Mars to be observed from the Earth at a global scale over the course of several hours. In this paper we report and analyse the occurrence of a bright and extended high-altitude detached layer identified during these observations.

2. Observations on 17 November 2020

A group of amateur astronomers (all co-authors of this study) was coordinated to carry out these observations. They were distributed in latitude and longitude in order to maximise the chances of favourable observations. The best conditions occurred in France where the altitude of Mars near culmination was around 50°. Two independent observers were able to follow the feature described here, namely Christophe Pellier (CP) and Emmanuel Beaudoin (EB). The seeing quality can be described by the Antoniadi scale[1]. Both CP and EB assessed a seeing number of 2/5 (defined as slight oscillation of the image with moments of calm lasting several seconds). This very good seeing is in agreement with the jet stream map of this night[2]. During this series of observations, the jet stream velocity was between 55 and 60 km h^{-1} with a west laminar flow coming from the ocean. These conditions are usually the best possible for ground observations in the north of France (Pellier et al. 2020). In most images the diffraction limit of the instruments is clearly reached in the red and green parts of the visible spectra. This is shown in Appendix A and in the first paragraph of Sect. 3.1.5.

2.1. Observation equipment

CP observed from Nantes (France, +47° 12 N, 1°33 W) using a 305 mm (12″) f/5 Newtonian telescope on an altazimuth mount, equipped with a ASI290MM monochrome CMOS camera, and an ASI224MC colour CMOS camera. The emission was detected above the same area with both cameras and various filters (UV, B 425, B 436, mainly broadband B). The exposures ranged from 5 ms (colour camera) to 100 ms (UV filter); the best 5–25% raw frames of all the videos were stacked to produce the

[1] https://en.wikipedia.org/wiki/Antoniadi_scalef
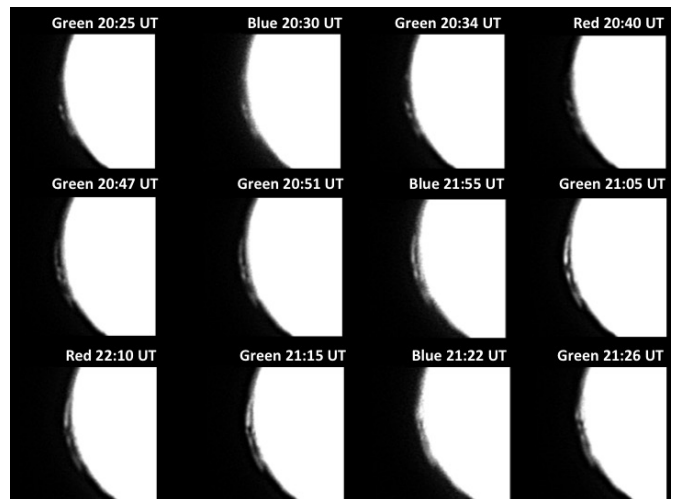[2] https://www.ventusky.com/?p=48.6;1.7;5&l=pressure

Fig. 1. Time evolution of the detached layer from 20:25 to 21:26 UT through red (R), green (G), and blue (B) filters. The disk is overexposed in order to better show the phenomenon (EB).

final images. CP was able to obtain reflectance (albedo) values of the atmospheric feature at five different bandwidths over the visible range and compared them to different typical areas of Mars.

EB observed from Palaiseau (France, +48°7 N, 2°23E) using a 356 mm (Celestron 14) Schmidt-Cassegrain on an Astrophysics 900 mount, with an ASI290MM camera. The sampling was of 0.09″ per pixel. The exposure time was 2.5 ms (red filter), 3.5 ms (green), and 8 ms (blue). The 10 to 20% raw frames were stacked to produce the final images. EB was able follow the atmospheric feature with 4–5 min time resolution over 3 h. The scale in both cases is 37.6 km per pixel.

2.2. Image processing

The images were processed by wavelets (or PSF Fourier transform), which is a systematic method to increase details in planetary imaging. We were able to control from the shape of the first-order diffraction rings around the bright edge limb that this processing did not deform details (intensity profile similar to the theoretical one).

EM videos processed with AutoStakkert!3, and details enhanced through wavelets with Astrosurface, similar for all the images in all three channels. In the case of overexposed images, an increase in contrast with the contrast slider was used to better show the cloud.

CP videos processed with AutoStakkert!3, and details enhanced through PSF and wavelets with Astrosurface.

2.3. Observations

An atmospheric feature, hereafter called a detached layer is present on all observational bands above the Mars terminator from 20:00 UT until about 23:00 UT. In the RGB image it shows a colourful shape where green and blue dominate. The layer is very well detached from the surface of the planet. Figure 1 shows the rapid dynamics. The structures change from frame to frame and rotate with the planet. Its dynamics are also visible on the non-saturated time frame taken with a green filter in Fig. 2.
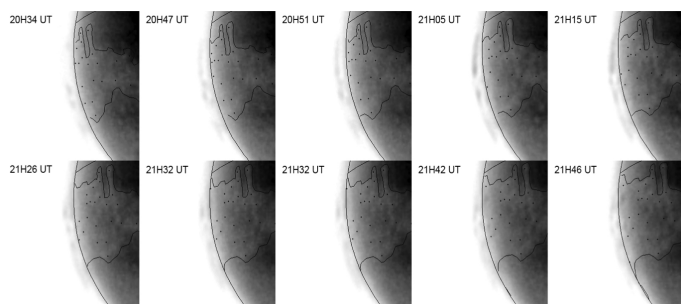
Fig. 2. Time evolution of the detached layer from 20:34 to 21:46 UT through a green filter without overexposure of the Martian disc (EB).
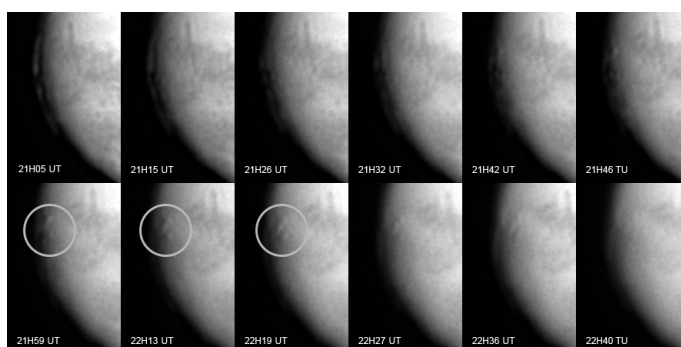

Fig. 3. Time evolution of the detached layer from 21:05 to 22:40 UT through a green filter without overexposure of the Martian disc. From 21:42 UT, the detached layers are clearly visible in front of the disc, and they cast shadows. The grey circles indicate their position for three different times (EB).

The detached layer seems to dissipate quickly when lit by the Sun, yet some distinct patches can still be seen in front of the planet near the terminator. Some of them are thick enough to cast shadows, as shown in Fig. 3.

To our knowledge, this was the first time that the complete dissipation of a Martian detached atmospheric layer at dawn was observed, from its illumination by the Sun until its complete disappearance. It was also one of the rare observations of a very large-scale structure at high altitude (Sánchez-Lavega et al. 2018). The detached layer occurred close to the western side of the main magnetic anomaly in the southern hemisphere, spreading over (50° S, 0° S) with longitudes between 218° and 295° W (142° and 65° E), extending over about 3000 km and consisted of a series of features not continuously linked with one another. At the same time, a cross-equatorial dust storm was occurring and was visible on the opposite side from these atmospheric features. It can be seen in Fig. 4 where we compare the colours of this dust storm (yellow) to that of the detached layer (greenish) at the same time.

3. Physical description of the detached layer

3.1. Detached layer altitude estimation

We compare in Fig. 5 the apparent altitude extent of the cloud with the expected diffraction spread assuming a thin source point cloud. To determine the image resolution, we extracted the Olympus Mons caldera and compared it to its actual size. We find a resolution of 3.4 pixels (see also Appendix A). The detached layer full width at half maximum (FWHM) is systematically between 3 and 3.5 pixels. The theoretical FWHM for a
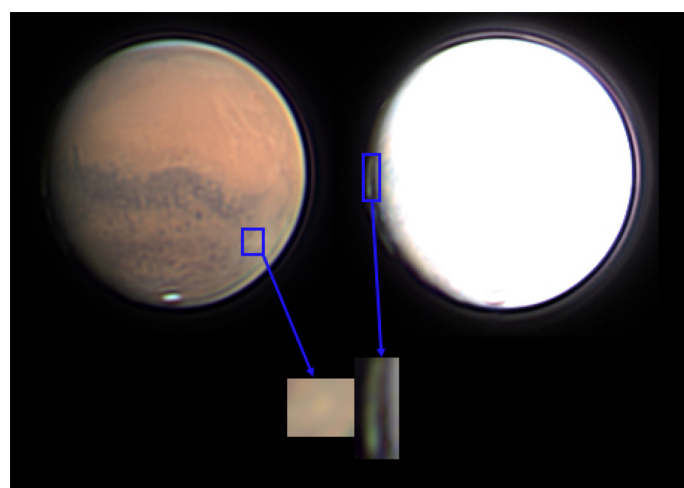

Fig. 4. Pictures of the planet Mars during the 17 November 2020 observation. *Left panel*: dust storm clearly visible in the southern hemisphere in this RGB image (2020-11-17 21:03.3 UT). *Right panel*: same image enhanced to see the detached layer (images of EB processed by JLD).
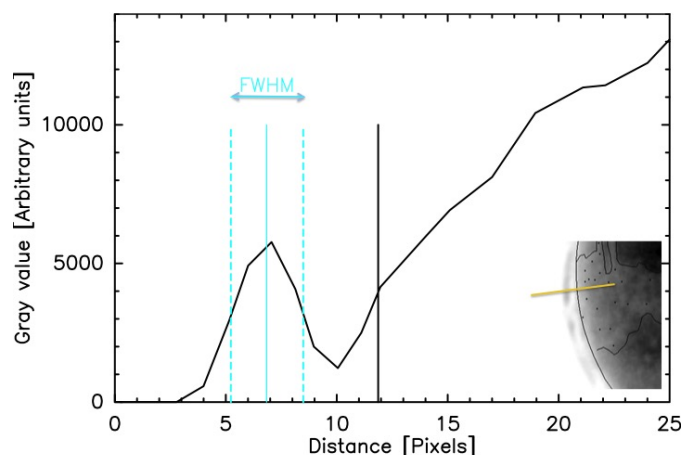

Fig. 5. Intensity profile of the detached layer at 21:05 UT. The black vertical bar shows the position of the terminator. The blue vertical solid line shows the position of the maximum intensity of the cloud detached layer with the full width at half maximum between the two dashed blue vertical lines. On the right side, a cartridge of Mars with the detached layer in the cross-section where the intensity profile was taken shows a thin cloud system emerging with a width similar to the point spread function (rather than a higher cloud located closer to the terminator) with an actual apparent width of 3.4 pixels (see text).

point source observed with the actual instrument used is 3.4 pixels (about 125 km) at green wavelengths. This suggests that what is observed is the point spread function (PSF) of a thin detached layer.

We used four different methods to estimate cloud altitude, two geometric and the two based on feature coordinates.

3.1.1. Method 1. 2D geometric method: Emergence from shadow

This is the first trigonometric approach, which allows the minimum and maximum altitude to be calculated. It can be compared to the approach presented in Hernandez-Bernal et al. (2021a), which proposes a systematic study of clouds observed during twilight on Mars with the Visual Monitoring Camera (VMC) on
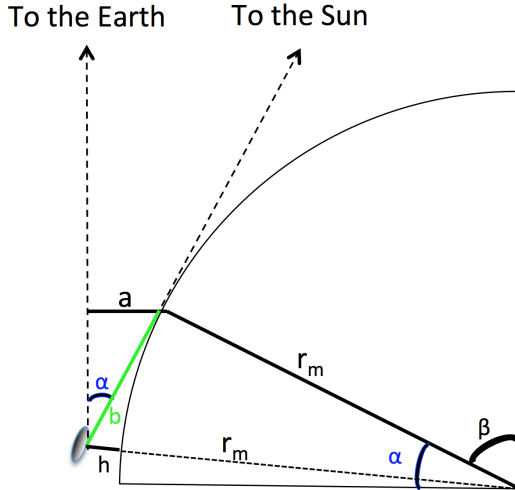
Fig. 6. Altitude determination with method 1: geometry of the altitude of the detached layer. The distance a is estimated from the images. Its value is 7.5 ± 0.5 pixels (i.e. 282 ± 18.8 km).

board Mars Express. However, our geometry is very different as we observe from the Earth. Our observational scheme is shown in Fig. 6. The time of observation allowed us to determine α, the angle between the Earth and the Sun direction at the detached layer. R_m is Mars radius. This estimation is done by using a cache with the correct Mars radius positioned exactly above Mars picture. The cache is positioned taking into account the planetary position, topography, and contour profile. We did not use the terminator because it does not represent the actual physical side of Mars. Therefore, the error on the surface location is smaller than a pixel, and only the error on the detached layer observation has to be taken into account.

The minimum possible altitude H_{min} is obtained when the detached layer is seen as soon as it is illuminated by the Sun. In this case, the distance between the terminator and the detached layer is $b = \frac{a}{\sin(\alpha)}$. As we have $(H_{min} + R_m)^2 = R_m^2 + b^2$, the minimum altitude of the detached layer is

$$H_{min} = \sqrt{R_m^2 + b^2 \frac{a^2}{\sin^2(\alpha)}} - R_m. \tag{1}$$

From the planetary geometry $\alpha = 23°$ and $\beta = 67°$, which gives b equal to 790 km. We can then calculate h, the height of the detached layer above Mars' ground, if we assume it is first observed once illuminated while emerging from the night side. We obtain h equal to 91 ± 8 km. Other assumptions regarding cloud location while first illuminated lead to higher altitudes, up to an unrealistic value of 311 km if the detached layer is first seen above the terminator.

3.1.2. Method 2. 2D geometric method: Shadow of the detached layer

This method is based on the shadow to detached layer apparent distances. As seen from the Earth, this method suffers from a large uncertainty, but still deserves some consideration. The main idea is to consider the distance between the edge of the layer and that of its shadow. It can therefore only be used when the detached layer is seen in the dayside just before it dissipates. The geometry is shown in Fig. 7. In this case, the shadow seen from the Earth is AC. It projects on H in the direction of the
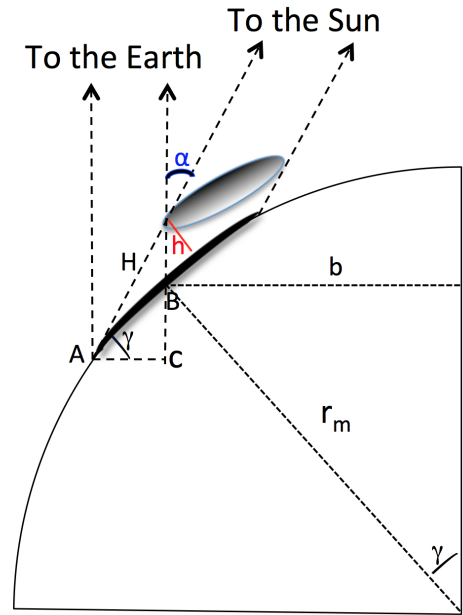
Fig. 7. Altitude determination with method 2: geometry to compute the altitude of the cloud with the second method. The altitude of the detached layer is h. The part of the shadow visible from Earth is AC, which projects on the AB segment on the surface of the planet, considered a plane at this scale, and γ is the angle between the perpendicular to this segment in B and the Earth direction

Sun so that $H = \frac{AC}{\sin(\alpha)}$ where $\alpha = 23°$. It is of course difficult to clearly determine AC in the images. However, we found a situation where it is clearly seen, with a value of 5 pixels (i.e. about 188 km).

The value of γ is determined at the centre of Mars as $\sin(\gamma) = \frac{b}{R_m}$. The value of b is also determined from the pictures. However, we also get in A the relation $h = H \cos(\alpha + \gamma)$. From this simple set of equations, we can easily determine the altitude h of the detached layer. The larger the shadow, the better the determination. The diffraction limit being 3 pixels, we should make a determination with values larger than that. In the set of frames, we found four cases with a shadow covering 5 pixels (i.e. a maximum of 190 km). An example is shown in Fig. 8 at 21:19UT. Here the value of b is 71 pixels (i.e. about 2700 km). With these values the altitude h is equal to 90 km. This altitude is that of the edge of the detached layer at time of the observation. The error bars are mainly due to the determination of the layer to shadow distance. Five pixels is above the diffraction limit. The error bar of ± 1 pixels results in a value of 90 ± 15 km. However, the dynamics of the phenomenon prevents us from finding enough cases to use this method with a high degree of confidence.

3.1.3. Method 3. 3D geometric method: Emergence from shadow

This method is based on the 3D equations (SL1 to SL19) in Sánchez-Lavega et al. (2015), and take into account the angle of illumination from the Sun and the angle of view from Earth (using subsolar point coordinates and Earth declination from Mars). For the sake of comparison, we used the same notations as in Sánchez-Lavega et al. (2015).

Looking at the time series of images (35 observations in red, green, and blue, spread over 2 hours, i.e. 30° in longitude), we can follow several stable faint features in the detached layer.
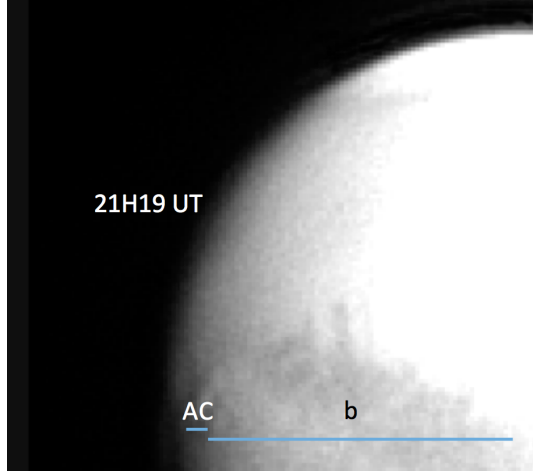
Fig. 8. Altitude determination with method 2: example of the determination of the detached layer altitude with the geometric method based on the shadow width (not to scale). The letters refer to Fig. 7.
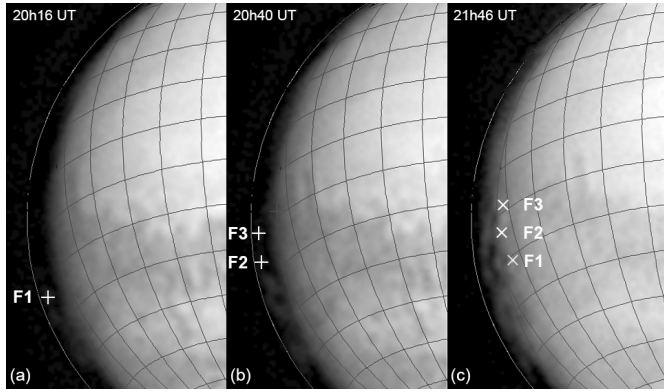

Fig. 9. Altitude determination with method 3. The features observed in the detached layer are used to determine its altitude (plus sign at the centre of the diffracted shape). The external white circle shows the position of the limb above the illuminated disc. *Left panel*: detection at emergence from the planet shadow of Feature 1 (F1). *Middle panel*: detection at emergence from the planet shadow of F2 and F3. *Right panel*: same features observed one hour later. The crosses (x) show the earlier measured feature positions at detection time having moved eastward with the rotation of the planet. F1, F2, and F3 are now on the cloud's western front (images by EB processed by MD). See additional movie S4.

They are visible below the limb on the morning night side of the planet, emerging from the planet shadow. Then they progressively rotate above the day side, appearing there as small clouds. The determination of the detached layer altitude is based on these features observations. Nine have been identified, three of which (called F1, F2, and F3) are shown in Fig. 9. The F1, F2, and F3 measured apparent positions (latitude, longitude when first observed) move with the planet rotation and their own dynamics. They appear at the eastern front of detached layer and become visible on the dayside after one hour (or 15° in longitude). In the following we suppose that their first occurrences are when they emerge from the shadow of Mars. If they formed closer to the terminator, this would result in a higher altitude estimation. Our assumption is therefore only the most conservative one that provides the lowest possible altitude estimation.

At any latitude we estimate the apparent longitudes at the time of emergence by measuring the centre of the appearing feature; if the cloud is just emerging it should look like a thin

Table 1. Altitude determination with method 3: calculated altitude (in kilometres) of the different structures measured on the 17 November 2020 images.

Feature	Altitude (km)
F1	88^{+31}_{-16}
F2	90^{+26}_{-16}
F3	98^{+32}_{-15}
Average	92^{+30}_{-16}

line, so we measure the centre as the feature is smaller than diffraction effect. This is illustrated in Fig. 9, left panel. These latitudes and longitudes are used to compute the angular distance between the structure and the limb (Eq. (SL1)). The apparent altitude z (or visible projected altitude, Eq. (SL8)) is calculated by measuring the apparent distance between the feature and the terminator. Using Eqs. (SL13), (SL15), and (SL19) in Sánchez-Lavega et al. (2015), we derive the Mars shadow altitude at the apparent longitude and latitude. Equation (SL12) allows us to deduce the altitude H_{MAX} if the structure is located at the terminator (instead of the apparent longitude and altitude on the night side of Mars).

Each structure is followed in the images from their first occurrence in the western night to the dayside of Mars in the east. This allows us to determine the evolution of the eastern front for three of them; when a cloud is seen with a lower angle, it is resolved so we do not consider the centre but the edge of the feature which emerged earlier (see right panel of Fig. 9). This is a very strong indication that the actual positions of the features are not located at the terminator (hence their altitude is not H_{MAX}), but rather at the apparent latitude and longitude on the night side, indicating these features were indeed emerging from the Mars shadow. The actual numbers are given in Table 1.

The measurements were performed at their centre and the error bars are estimated by considering two uncertainties. The first is the uncertainty in the estimation of the timing of emergence of the feature. It actually emerged from the shadow of Mars between the image where it was first observed, and the previous one (where it was not observed). We hence consider a time uncertainty of half of the time separating the two images (around −2.5 min), which translates into a longitude uncertainty of −0.6°. The second is the uncertainty in measuring the positions in pixels, estimated to ±0.5 pixel.

These uncertainties are introduced into the equations to calculate the error bars of the altitude estimates. We finally obtain the results described in Table 1. On average, the detached layer altitude is 92^{+30}_{-16} km, with one of the features reaching 98 km (+32/−15 km). Should the different features used to compute it show up closer to the terminator, this altitude would be still higher, as explained above. Taking all nine observed features into account results in the same estimate.

3.1.4. Method 4. Following the cloud position over time and calculating its altitude

Sánchez-Lavega et al. (2015) first measured the projected altitude of the top of the feature (called a plume) as projected onto the dark background at the limb in all images over time, assuming that its shape remains stationary over the time of observation. Their other assumption is that the plume crosses the limb when
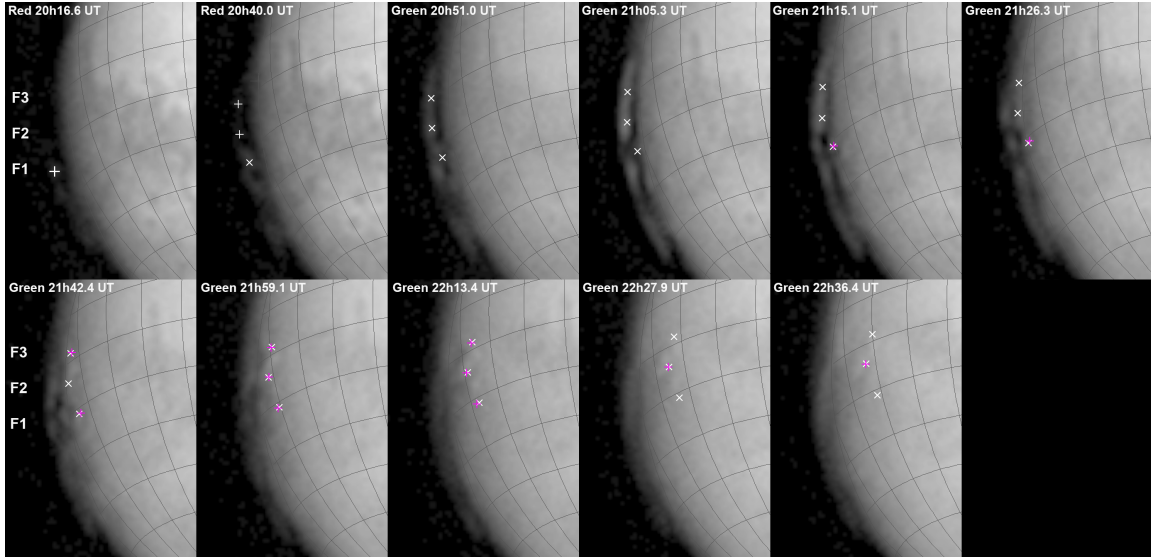
Fig. 10. Altitude determination with method 4: time evolution of three features F_i on the cloud. The F1 emergence position is shown as the white plus sign (+) at 20:16 UT (*top left*). The F2 and F3 emergence positions are shown as the white plus signs at 20:40 UT (*top, second image from the left*). The white crosses (x) on all observations indicate the emerging positions of the features reported on the observation times (taking into account the eastward rotation of the planet). Finally, the pink plus signs from 20:51 UT to 22:36 UT correspond to the measures of the respective features of the eastern cloud front, closest to and at the same latitude as the emerging position.

this altitude is the highest in order to determine the cloud coordinates through a pair of latitude and longitude coordinates. These coordinates were used in the equations to simulate the projected altitude for all images over time. When the planet rotates, they measure the feature's projected altitude and fit a polynomial on this temporal series to determine an upper altitude. They finally compare this fit to models of the projected altitude that would result from a feature of different altitude approaching the terminator and rotating into view for the Martian viewing geometric condition.

This approach cannot be applied in the same way in our case as here we do not have a simple cloud with a clearly identified position (e.g. the highest part of the cloud). The 17 November 2020 observations show a very complex and dynamic cloud system making it difficult to identify exactly the same part of the cloud (measured at emergence) without any additional input (see Sect. 3.1.3.)

Nonetheless, the SL equations are correct in our case. In particular, Eqs. (SL18) and (SL19), which take into account the tilt of Mars' rotation axis, allow us to determine the altitude of the planet shadow for any set of latitude and longitude coordinates. Even so, it is possible to follow the altitudes of the three features F_i discussed in Sect. 3.1.3. From 21:25 UT to 22:60 UT, we determine their longitude and latitude at 15 different times using the Winjupos software. These are used as inputs in equations SL to determine the evolution of their altitudes.

This time evolution is shown in Fig. 10. The plus sign in the first two panels (from the left), top row, shows the emergence of the features F_i. We follow this east front for each feature at a constant latitude and determine its longitude $Long_t(F_i)$ in each frame, taking into account the intrinsic rotation of the planet. These observations (after emergence) are shown as crosses in Fig. 10.

The uncertainty on $H_{t_o}(F_i)$ is not the same than for $H_t(F_i)$. In both cases, we must account for the pixels uncertainty, estimated to ±0.5 pixel, i.e. ±16 km) as in Sect. 3.1.3. However, the exact time of emergence is unknown and may be any time between the
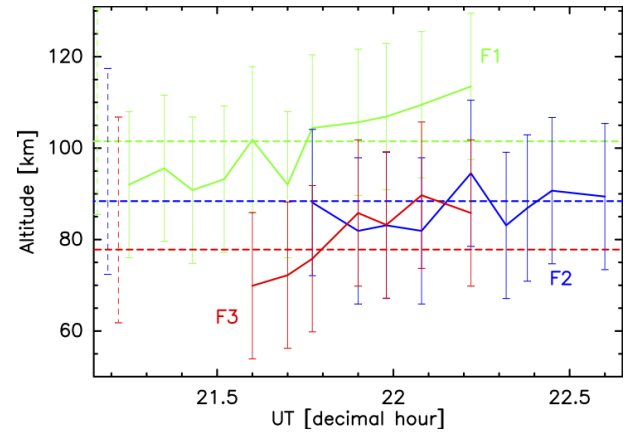

Fig. 11. Altitude determination with method 4: results of the altitude determination using the method described in Sect. 3.1.4. The abscissa is the decimal hour. The three features followed here are the same as in Sect. 3.1.3. The solid lines represent the estimated altitudes of the features (green: F1, blue: F2, red: F3) over time after emergence. The error bars are ±16 km. The dashed lines represent the estimated altitude at emergence. Their error bars are $^{+29}_{-16}$ km. They are shown at the beginning of this figure for the sake of clarity. In decimal hours, the exact times of emergence are $t_o(F_1) = 10.16$, $t_o(F_2) = t_o(F_3) = 10.67$, i.e. outside the abscissa range.

preceding frame (when the feature was absent) and the first time when the feature is seen. The error bars become asymmetric with values $^{+29}_{-16}$ km.

The altitude results are shown in Fig. 11. Considering the error bars, the altitudes $H_t(F_i)$ over time fit well with that at the emergence $Ht_o(F_i)$. $H_t(F_2)$ remains approximately constant. A gradual increase is seen for $H_t(F_1)$ and $H_t(F_3)$. However, great care should be taken when trying to interpret it in terms of wind as the data are very sparse. Averaging $H(t(F_i))$ results in an altitude of 89 km (see Table 2).

Table 2. Altitude determination with method 4: calculated altitude (in kilometres) of the different structures measured on 17 November 2020 using the second 3D method.

Feature	$\sum \frac{H_{\text{measured}}^{\text{obs}}}{n_{\text{obs}}}$	$H_{\text{emergence}} - \sum \frac{H_{\text{measured}}^{\text{obs}}}{n_{\text{obs}}}$
F1	100	+1.5
F2	86.6	+1.7
F3	80.3	−2.5
Average	89.0	+0.3

3.1.5. Discussion on the altitude estimate

The four methods lead to comparable results, with overlapping uncertainty ranges. We decided to keep the estimate of the third method (92^{+30}_{-16}) km for two reasons. Firstly, this method relies on altitude estimates over various cloud features; the uncertainty range represents both the individual uncertainty estimate and also the possible actual cloud system altitude variability. Secondly, it has the largest uncertainty range and includes most of the uncertainty ranges of the other methods.

3.2. Estimation of the colour profile and albedo of the detached layer

Our intention was to measure the geometric albedo of the detached layer in order to determine its colour profile. We performed UBVRI photometry of the planet following the AAVSO method, using three reference stars observed at the same airmass (Zeta Pegasi, Epsilon Piscium, and HIP 682). Following Schmude (1992) we calculated the normalised magnitudes of the planet (as if observed at 1 astronomical unit (AU) from the Sun, and 1 AU from the observer). Following Mallama (2007) we corrected the magnitudes from orbital parameters, allowing the calculation of the geometric albedo at a solar angle of 0°, thanks to an equation from the same paper. From Mallama (2007) we verified the precision of the results. The VRI magnitudes are correct, while U and B are slightly fainter than the references, this coming either from imprecision or from a real situation (when observed, the planet was lacking the usual bright short wavelength features such as a wider polar cap or white clouds), or both. Finally, the results reach an acceptable precision in order to retrieve the albedo differences of the measured details (Fig. 12).

This results in a geometric albedo (as in McCord et al. 1971) which is the equivalent of the I/F ratio between the radiance coming from the surface in a given direction (in W m^{-2} sr^{-1}) and the incident flux coming from the Sun arriving perpendicularly on the surface (in W/m^{-2}) (Vincendon et al. 2007). We focussed on four different Martian details, whose intensity was normalised as if they occupied the same area as the whole planet: Amazonis, a bright desert in the north; Valhalla, a reddish north–south geological delimitation of particular albedo; Mare Cimmerium, a vast region of dark albedo to the south; the south polar cap. We compared these spectra to the detached layer (terminator feature in Fig. 12) and to the global albedo of the planet as reference.

The analysis correctly describes the features visible in the images, for example the fact that Mare Cimmerium is less luminous than the planet in total or that Amazonis is very bright (spectrum that goes up intensely towards the IR). Likewise, the albedos are very close in U and B (the planet displays a flat contrast). The polar cap presents an unexpectedly low albedo because it is observed at a grazing sunlight angle (15°) and the
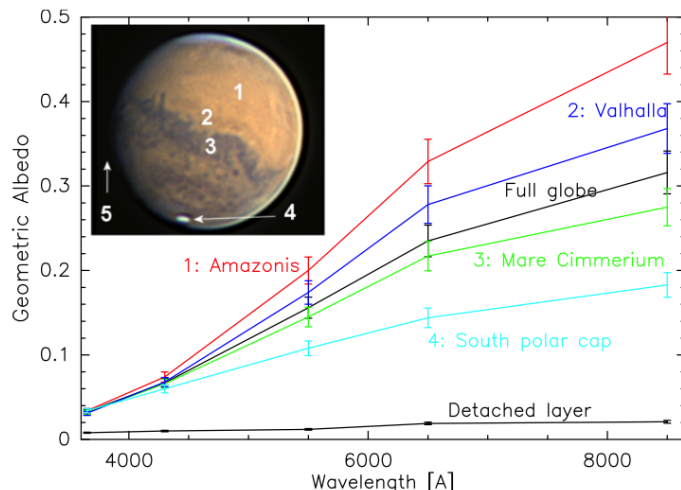

Fig. 12. Albedo of different Martian structures compared to those of the full globe and of the observed terminator feature for 17 November using a 305 mm F/5 Newtonian and an ASI183 mm Pro Camera (credit CP). From top to bottom: Amazonis (red line), Valhalla (dark blue line), full globe (black line), Mare Cimmerium (green line), south polar cap (light blue line), and the studied detached layer (black line). These values are corrected from orbital parameters: solar phase angle of 27°, rotation angle 192°, orbital longitude (Ls) 316°. From left to right, the UV filter covers the range [3250–4000 Å], the blue filter [3780–4750 Å], the green filter [4780–6025 Å], the red filter [5870–7120 Å], and the IR filter [7250–10 000 Å]. Their normalised magnitudes for $\alpha = 0°$ are 0.87 (UV), −0.04 (B), −1.61 (G), −2.45 (R), and −3.09 (IR).

results are not corrected from the gradient of light across the disc.

These results are in good agreement with McCord et al. (1971) and Bell et al. (1997). Both articles propose the same geometric albedo (or I/F in the second one) for different Martian structures with a similar increase in wavelength and comparable values.

This albedo spectrum represents how the solar light is reflected by a given structure. For qualitative purposes only, an enlargement of the detached layer can be seen in Fig. 4. The detached layer is characterised by a reflectance increase by a factor of two from blue to red. This increase is lower compared to typical Martian terrains, notably bright terrains covered by dust over which the ferric oxides result in an increase by a factor greater than 5.

3.3. Estimation of the size and optical depth of particles constituting the layer

The colour analysis discussed above suggests that the detached layer scatters light at all visible wavelengths, with a maximum in the red; this does not correspond to molecular Rayleigh scattering or single wavelength emission, while it suggests a layer composed of dust aerosols or ice crystals. The wavelength dependence of scattering at visible wavelengths is strongly sensitive to particle size. We used radiative transfer simulations results from Vincendon et al. (2011), available at wavelengths larger than 0.5 µm to estimate the mean size (effective radius) of the particle distribution of the layer. We assumed either a CO_2 or H_2O ice composition; however, as discussed below, the detached layer does not seem to be easily compatible with dust owing notably to its altitude. We first calculated ice single scattering properties of spherical particles using Mie theory, and then
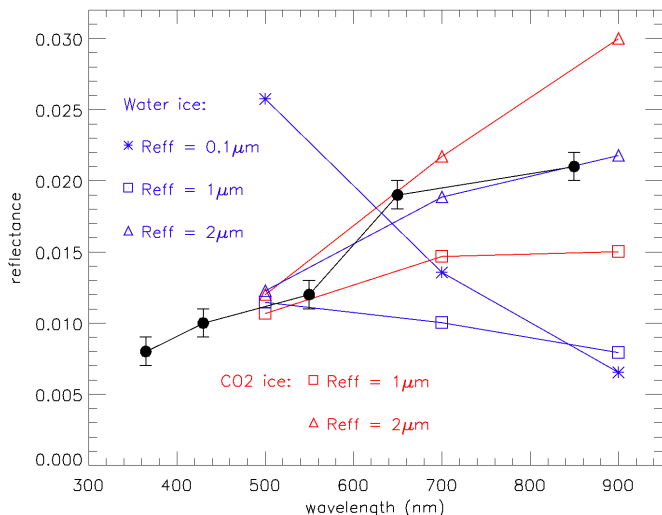
Fig. 13. Spectrum of the detached layer derived from Fig. 12 (black dots) compared to scattering models of CO_2 (red) and H_2O (blue) clouds with various ice crystal particle sizes (effective radii: squares, 1 µm; triangles, 2 µm; stars: 0.1 µm). Models are from Vincendon et al. (2011) for the following visible optical depths (at a wavelength of 0.5 µm): 0.5 (red triangles), 0.35 (blue triangles), 0.2 (squares), 0.15 (blue stars). The observed cloud is either compatible with CO_2 particle sizes in the 1–2 µm range or water ice particle sizes of about 2 µm.

computed the radiative transfer within a plane-parallel homogeneous layer of particles (see Vincendon et al. 2011 for details). The results are presented in Fig. 13, and are broadly consistent with those presented in a recent study using another modelling approach (Clancy et al. 2019). In particular, we observed that the visible range is very sensitive to particle size: small-grained ice clouds (effective radius lower than 0.5 µm) have a decreasing reflectance with increasing wavelength, while larger-grained ice clouds (effective radius greater than 1 µm) have a flat to increasing reflectance with increasing wavelength. The model was initially developed for nadir viewing data analysis where surface and atmosphere are in the field of view. However, cloud-only reflectances were derived in Vincendon et al. (2011) using a totally absorbing surface. Such a configuration is comparable to our viewing geometry where either free space or surface on the night side is in the line of sight beyound the cloud. The viewing geometry was nadir (null emergence) and a 45° solar zenith angle. This is very close to the actual viewing geometry of the data analysed here with a 23° phase angle. The main difference is related to the meaning of the optical depth used in the model, which corresponds to the optical depth along the line of sight, and not to the normal cloud optical depth.

The observed layer is characterised by an increasing reflectance trend with wavelength. This is clearly not compatible with particles sizes lower than 1 µm according to results of Fig. 13 or to other studies (Clancy et al. 2019); the wavelength dependence corresponds to ice particles typically in the 1–2 µm range. The main source of uncertainty here is linked with the potential biases of the reflectance data points (in black in Fig. 13) on which we try to fit the model. The relative consistency of filter response was appreciated using spectra gathered all over Mars (Fig. 12), but we cannot exclude here some sort of systematic biases that may distort the cloud spectral shape whose flux is significantly lower compared to other points on Mars.

This modelling section also allows optical depth to be estimated. Cloud reflectances are between 0.01 and 0.02 over the visible range. According to the model (Fig. 13), this corresponds

to an optical depth in the 0.2–0.5 range in the visible (wavelength 0.5 µm). This can be compared to two CO_2 clouds analysed in Vincendon et al. (2011) where slightly lower reflectances (from which background from the surface were removed, so comparable to this study) increasing from 0.007 to 0.11 and from 0.012 to 0.016 were modelled by optical depths of 0.17 and 0.22, respectively (see their Fig. 13). We note however, as discussed previously, that the geometry is not comparable as we are deriving optical depth along the slice of the cloud, and not normal optical depth. We also note that cloud brightness is spread over several pixels by diffraction, which impacts the optical depth estimate from radiance measurements.

4. Interpretation of the detached layer

Although rarely reported from the Earth, Martian bright detached layers are commonly observed by spacecraft. They are composed of ice and/or dust particles and are referred to as 'clouds'. One of the first reports comes from Jaquin et al. (1986), who mentioned several decades ago a detached layer up to 80 km in height at Ls = 210°. A recent review of the Mars clouds is provided in Haberle et al. (2017). The authors distinguish three kinds of upper altitude clouds: (i) trail clouds occurring at 10–35° S, for solar latitudes of 240–270°, which are not compatible with our observations; (ii) equatorial CO_2 clouds, most of which are concentrated between 10° S to 10° N, while we observe our clouds extending down to 50° S; (iii) diffuse and layered hazes that can occur at Ls = 316° (our case), at altitudes between 60 and 110 km, and at latitudes between 50° S and 50° N, both of which are compatible with our observations, although the morphology of the layered structures, with horizontal scale of less than about 100 km, are not directly comparable to our observations. Recently, Mars Express VMC observations gathered over 14 yr have been analysed by Hernández-Bernal et al. (2021b) to provide an overview of Martian high-altitude clouds. These VMC observations possess a large field of view, and the study focusses on twilight clouds; their results are particularly relevant here. We can see in their Fig. 3 that they report only a few occurrences of clouds at our longitude of about 100° E. Only one is large scale (100 000 km²), but it is located in the 50–60 km altitude range. This suggests that the bright detached layer reported in the present study is relatively atypical. As we are not able to assess spectroscopically the composition here, we examine in more detail various potential explanations in the next sections.

4.1. Auroral assumption

Bertaux et al. (2005) discovered the Mars aurora through its UV emission with the SPICAM instrument (Bertaux et al. 2000) on board Mars Express (ESA). Electron aurora typically peak at an altitude of 130 km, with widths ranging between 120 and 150 km (Dubinin et al. 2009; Lilensten et al. 2015). Proton aurora peak at an altitude between 120 and 150 km, with half widths ranging from 110 to 170 km (Deighan et al. 2018; Ritter et al. 2018). Solar energetic particle (SEP) precipitation allows this altitude to drop to 110 km (Jolitz et al. 2017), and to 50 km during extreme active SEP events (Haider & Masoom 2019). Lilensten et al. (2015) predicted experimentally and theoretically that visible aurorae should occur in the atmosphere of Mars at around 140 km (blue and green) and 160 km (red) for a 100 eV electron input flux energy. These typical predicted altitudes of auroral emissions are significantly greater than the altitude of the feature analysed here, which indicates that the detached layer is not compatible

with aurora. Additionally, the spectral properties of our bright feature are not consistent with theoretical expectations for aurorae, which should be less intense at high wavelengths compared to the blue values, in particular in the near-IR (850 nm). More precisely, following the model, the integrated red line intensity should be 2.82 times stronger than the blue band value, and the integrated green line intensity 10.1 times stronger than the blue value in a Martian aurora (Lilensten et al. 2015). While the first ratio is compatible with the detached layer described in this work, the second is not. Finally, we also note that the solar conditions on Mars were quiet with no evidence of SEPs (see EUHFORIA simulations in Appendix B; Pomoell & Poedts 2018).

4.2. Elevated dust clouds assumption

The cloud system is observed at $L_S = 316°$, a timing compatible with 'C storms' corresponding to the last stages of the storm season (Kass et al. 2016). As noted above, a large cross-equatorial regional dust storm is actually present at the opposite side from the detached layer, which demonstrates that dust lifting activity occurred at the time of observation and raises the question of a possible dust composition of the detached layer. Figure 4 shows that the apparent colours of the dust storm are not similar to those of the detached layer, and Fig. 12 shows that the reflectance properties of the layer are significantly less red than the dust-covered terrains of Mars. These colour considerations suggest that the layer may not be primarily composed of dust. In terms of altitude, most dust hazes or layers are reported or expected to extend typically to a maximum altitude of 50–60 km, or perhaps up to 80 km during extreme events such a global dust storms (Spiga et al. 2013; Smith et al. 2013; Heavens et al. 2014; Stcherbinine et al. 2020). However, in that case dust is not present at such a high altitude as a detached layer: dust spans continuously from low to high altitudes, with a decreasing scattering intensity, while our observations clearly show a gap of several tens of kilometres between the clouds and the ground (Fig. 5).

Hernández-Bernal et al. (2019) report on the 2018 Martian global dust storm over the southern polar region. They mention long and narrow aerosol curved arcs with a length of about 2000 to 3000 km traversing part of the cap and crossing the terminator into the night side, but at an altitude lower than 40 km. They also report that the maximum altitude of aerosols occasionally reaches 70 km at moderate latitudes, but again in the form of a continuous dust haze and not a detached layer. Montmessin et al. (2006b) also mention that the haze top depends on the seasons and latitude, with a maximum for L_S 180° to 250°, between 0° and 30° S, while our layer is observed at L_S 316°. The properties of the cloud system thus seem weakly compatible with a high-altitude dust layer explanation according to these previous studies. The composition of the observed layer is therefore most probably ice. However, we show below that dust could still play a small role by enhancing the scale height and/or creating high-altitude nucleus kernels.

4.3. Water ice clouds assumption

Laterally extended water-ice clouds spanning 6000 km, thus comparable to our cloud, have been reported recently during the Mars year 34 global dust storm (Connour et al. 2020), but at altitudes below 40–50 km. Smaller extent water ice clouds are detected all year round at altitudes greater than 50 km, and tend to be observed at higher altitude during southern spring and summer (Clancy et al. 2019), seasons compatible with our
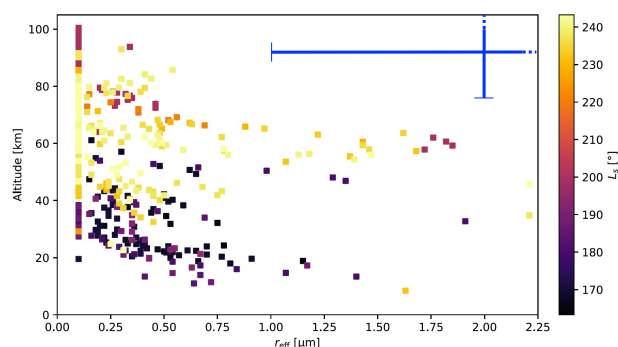

Fig. 14. Figure adapted from Stcherbinine et al. (2020) showing the 17 November cloud studied in this paper (in blue, with error bars) compared to the distribution of morning and evening H_2O clouds derived by Stcherbinine et al. (2020) during the 2018 global dust storm, represented in an altitude vs. effective radius plot.

observations. At very high altitudes (greater than 80 km) water ice clouds were initially thought to be improbable considering a needed water mass mixing ratio poorly compatible with an atmosphere dominated by CO_2 (Montmessin et al. 2006a). However, reliable spectroscopic observations of water ice clouds have recently been reported at altitudes reaching 80–90 km (Vincendon et al. 2011; Clancy et al. 2019), and even 100 km when they are associated with the extreme conditions of global dust storms (Stcherbinine et al. 2020). Water ice clouds can thus be located at the same altitude as our observed detached layer. However, all reported high-altitude (>70 km) water ice clouds are made of small particles with effective radius in the 0.1–0.5 µm range (Clancy et al. 2019; Stcherbinine et al. 2020). As discussed previously, the observed cloud spectral properties are compatible with a 1–2 µm effective radius, more precisely 2 µm in the case the cloud is composed of water ice crystals (Fig. 13). It is clearly not compatible with a particle size smaller than 0.5 µm. In Fig. 14 we compare our cloud to previous terminator observations (morning or evening) obtained during the 2018 global dust storm using ExoMars-TGO and presented in Stcherbinine et al. (2020). The error bars of our Earth-based retrievals are large, but we can see that the cloud detected here is located beyond the reported water ice clouds in the altitude versus particle size plot; compared to previously reported water ice clouds, our detection is either too high considering its particle size or too large-grained considering its altitude. This may indicate that water ice is not an appropriate explanation for this cloud. Alternatively, it may indicate that we are observing a relatively atypical water ice cloud. Water ice is indeed a relevant explanation for the season and latitude of our observation according to Clancy et al. (2019). Moreover, our large error bars come close to the distribution of water ice clouds shown in Fig. 14 and unidentified systematic biases may bring our observation even closer to known water ice clouds. It should finally be noted that the water ice cloud identification procedure of Stcherbinine et al. (2020) cannot capture water ice clouds with effective radius greater than 2 µm, due to possible confusion with dust. Such water ice clouds may thus exist occasionally, while not being represented in their diagram.

4.4. CO_2 ice cloud assumption

In contrast to water ice clouds, CO_2 ice clouds are known to form with large grain sizes at high altitude (Clancy et al. 2007, 2019; Montmessin et al. 2007; Vincendon et al. 2011; Määttänen et al. 2010). More precisely, the detached layer has visible spectral
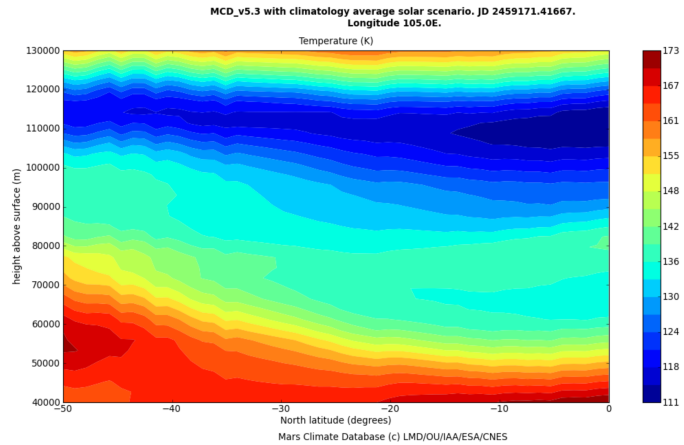
Fig. 15. Figure extracted from the Mars Climate Database (Forget et al. 1999; Millour et al. 2019) showing the vertical profile of atmospheric temperature as a function of latitude over a range covering our cloud (equator to 50° S), at a representative longitude of 105° E. The simulation corresponds to an Earth date of 17 November 2020, 22:00 UTC.

properties consistent with grain sizes in the 1−2 µm range for CO_2 ice and visible optical depths in the 0.2–0.5 range according to our modelling results (Fig. 13). This is typical of known mesospheric CO_2 clouds observed during the daytime. However, the reported spatial extents of large CO_2 clouds are typically hundreds of kilometres, sometimes reaching widths of 1000 km (Montmessin et al. 2007; Määttänen et al. 2010; Vincendon et al. 2011). The cloud system discussed here, about 3000 km wide, is significantly larger, although observational biases (e.g. reduced field of view) may limit the apparent extent of cloud systems observed from orbit. Additionally, our cloud occurs at times and places that do not correspond to the typical area of known CO_2 clouds (Montmessin et al. 2007; Clancy et al. 2007; Vincendon et al. 2011; Määttänen et al. 2010). Most daytime CO_2 clouds are reported between L_S 0° and 150° (Määttänen et al. 2010; Vincendon et al. 2011), which is during the non-dusty Mars season, while our observation was obtained at L_S 316° and at the same time as a large regional dust storm (Fig. 4). However, one occurrence of equatorial CO_2 clouds at a nearby L_S of 329° have already been noticed (Määttänen et al. 2010), which indicates that CO_2 cloud formation may sometimes start during mid-summer, when our cloud was observed.

We show in Fig. 15 the expected atmospheric temperatures at the time and place of our observations derived from the Mars Climate Database (MCD; Forget et al. 1999; Millour et al. 2019). These temperatures can be compared to the CO_2 frost point (Määttänen et al. 2010; Spiga et al. 2012), which typically decreases from 100 to 90 K as altitude increases within our uncertainty altitude range. Near the equator, where the cloud features are the most intense, the MCD simulation predicts temperatures of about 125 at 92 km, which decreases to about 110 at 110 km. According to Spiga et al. (2012), gravity waves are expected to decrease the temperature by typically 12 K compared to MCD predictions, which could bring atmospheric temperatures below 100 K within our uncertainty altitude range. Atmospheric temperatures may thus be compatible with CO_2 ice saturation, although at the margins. Actually, it has previously been shown that temperatures predicted by the MCD where and when CO_2 clouds are observed are typically 10–15 K above saturation (Määttänen et al. 2010). We can see in Fig. 15 that the coldest temperatures tend to be predicted at higher altitude
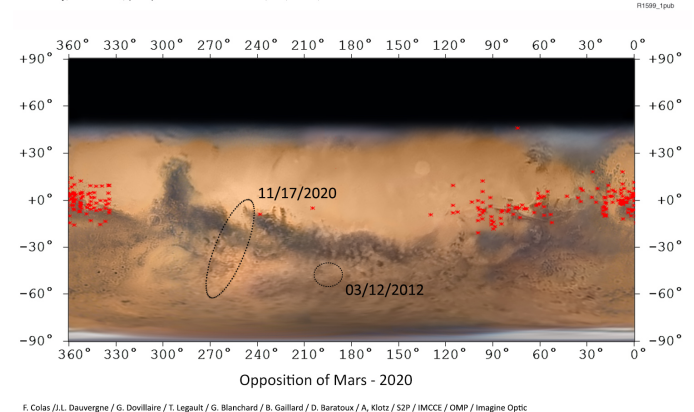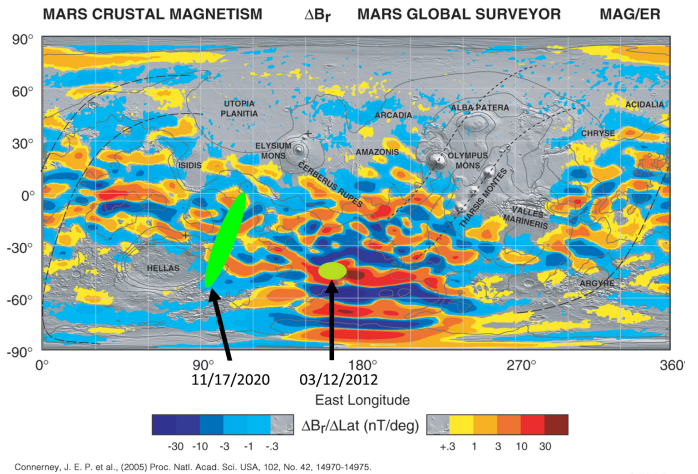
Fig. 16. Localisation of the cloud observed in this study (17 November 2020) versus those of the clouds reported in the literature. *Upper panel*: observation reported in this study localised on Mars (bright green) and compared to the magnetic anomaly. Also plotted is the observation in Sánchez-Lavega et al. (2015) on 3 December 2012 (pale green). The magnetic map comes from Connerney et al. (2005). *Lower panel*: previous detections of CO_2 clouds (red stars) (Clancy et al. 2007; Määttänen et al. 2010; Vincendon et al. 2011) projected on an albedo map, compared to the actual detached layer observation.

(110 km) in the MCD simulation compared to our average cloud altitude of 92 km. In addition to our wide uncertainty range, we also note that Montmessin et al. (2006a) similarly observe that the cold CO_2 ice compatible temperatures tend to be observed above, and not at the same altitude as bright detached layers interpreted as CO_2 clouds.

We compare in Fig. 16 the spatial distribution of the present detached layer with that of daytime CO_2 clouds from Montmessin et al. (2007), Määttänen et al. (2010) and Vincendon et al. (2011). The equatorial part of our extended cloud system is compatible with a few previous CO_2 cloud detections reported at comparable longitudes (Fig. 16). However, most of the cloud system seems to be located outside previously reported CO_2 cloud areas. This may be related to the difference in local time; our cloud was observed at dawn, while most observations of Fig. 16 were obtained during afternoon hours (a few OMEGA observations were acquired early in the morning (see e.g. Määttänen et al. 2010)). Alternatively, this may indicate that our cloud system is composed of H_2O ice and not CO_2 ice.

Another potential difference between our cloud and known CO_2 clouds is related to the altitude: 90 km is higher than the statistics provided in Määttänen et al. (2010) who report upper altitudes of 80 km for the top of the clouds. This may again

be explained by the fact that our cloud formed on the night side. CO_2 cold temperatures are indeed expected to be typically 10 km higher, reaching 90 km, at nighttime compared to daytime (Määttänen et al. 2010). This is fully consistent with our observations. Finally, it should be noted that nighttime CO_2 clouds have also been tentatively reported based on temperature consideration, but without spectroscopic confirmation, some at comparable L_S to ours (Jiang et al. 2019). This confirms that expected temperatures on the night side can be compatible with CO_2 cloud formation. These are however very small-grained (≤ 0.1 μm), a size not compatible with our cloud (Fig. 13).

Overall, it appears that CO_2 ice cloud formation may also explain our observation, although our cloud does not strictly correspond to any of the previously reported clouds.

5. Discussion

Our cloud is observed during the last stage of the storm season (L_S 316°) and at the same time as a regional dust storm (Fig. 4). The co-occurrence of the dust storm may be related to the fact that dust storms tend to enhance the atmospheric scale height, thus allowing dust (which can act as a condensation nucleus) and ice particles to reach higher altitudes (Clancy et al. 2019; Stcherbinine et al. 2020). In particular, large-grained water ice clouds were observed up to 70 km during the 2018 global dust storm (Stcherbinine et al. 2020). Our observation may then indicate that large-grained water ice clouds can reach altitudes even greater than the previously reported limit of 70 km.

Alternatively, the co-occurrence of the dust storm, observed on the other side of the planet, may be fortuitous and the cloud may be composed of CO_2 ice. Spiga et al. (2012) suggest that gravity waves could explain how CO_2 ice can form at high altitudes. Listowski et al. (2014) study the micro physics of CO_2 ice clouds, following the idea that gravity wave propagation allows for the creation of supersaturated layers (called cold pockets) able to initiate nucleation and to maintain growth of CO_2 ice crystals. They show that the cloud evaporates quickly after the cold pocket has vanished, which is similar to our observations. Typical high-altitude CO_2 ice clouds are, however, essentially not detected during the dust storm season when the overall atmospheric temperature is higher. The lack of dust at high altitude during a typical CO_2 cloud formation time frame (the cold, clear season) lead Listowski et al. (2014) to suggest that these clouds need an exogenous supply and to mention a possible meteoritic flux.

The 17 November observation occurs on the west side of the southern magnetic anomaly. This may just be a coincidence; the scarcity of favourable observation conditions makes it impossible to consider it a permanent feature. Still, we may question what mechanism could link these clouds to the magnetic field (Fig. 16). This question is also addressed in Andrews et al. (2016). These authors examine the Mars plume event of March–April 2012 (Sánchez-Lavega et al. 2015), and conclude that during this event the ionosphere experienced a disturbance above the magnetic anomaly (where the plume was observed) that could correspond to a large interplanetary coronal mass ejection encountering Mars. Our case is different from that of the plume, however, also because it happens at the border of the magnetic anomaly, while the plume was located within this anomaly (see Fig. 16).

A possible link lies in galactic cosmic rays (GCRs). Protons with energy of about 10^7 eV have a Larmor diameter (considering a magnetic field of about 100 nT) close to the latitudinal size of the magnetic anomaly (about 7000 km). On

Earth, the role of cosmic rays as nucleation precursors through ionisation has been a topic for many research projects after the seminal work of Svensmark & Friis-Christensen (1997). Curtius et al. (2006) showed that ions act as nucleation cores for the attachment of the supersaturated gas phase molecules. Such mechanisms have been shown to be efficient on Titan (Imanaka et al. 2004; Gronoff et al. 2009a,b) where cosmic rays trigger aerosols (Lavvas et al. 2012) that are 'the key to understanding Titan's lower ionosphere' (Molina-Cuberos et al. 2018). Although Titan's atmospheric chemistry is different to that of Mars, the fact that the observed Mars detached layer occurs west of the magnetic anomaly suggests that these mechanisms could also be at work. This has also been studied on Venus (Nordheim et al. 2015), where the absence of a magnetic field makes the GCRs penetrate straight into the atmosphere, while the Mars magnetic anomalies create a large gyration and may induce a slow-down through magnetic mirroring.

This mechanism is not contradictory with the possible presence of dust in the upper atmosphere linked with the simultaneous regional dust storm (Haberle et al. 2017): this dust may easily get ionised by incoming cosmic rays and become efficient nucleus kernels. Such mechanisms have been widely documented for example for interplanetary molecular clouds or discs around young stars (Nordheim et al. 2015). It is also consistent with the disappearance of the clouds in the daylight. There, the direct excitation and ionisation by the solar extreme ultraviolet radiation (Maret et al. 2006) gets much stronger than that from the precipitation. It could also contribute to explaining the unique observation made in 2012 above the Mars magnetic anomaly (Fig. 16), estimated at a higher altitude of 200 to 250 km (Sánchez-Lavega et al. 2015). On 17 November 2020, the solar conditions on Mars were relatively quiet, favouring the entry of cosmic rays. This new cloud and its complex interplay with dust and magnetic terrain thus provide new observational constraints that should help in deciphering the nature and properties of condensation nuclei responsible for high-altitude cloud formation on Mars.

6. Conclusion

For the first time a huge cloud system emerging from the Martian night could be followed continuously from the Earth, from its appearance at the terminator until its complete dissipation. Such time-resolved observations of an unpredictable phenomenon were made possible by the use of telescopes from Earth, as a dozen observers followed the evolution of a dust storm on the opposite edge of the disc. This constitutes strong evidence of the need to complement in situ probe observations by extensive and regular Earth-based observations. It also shows (once again) the power of professional and amateur collaboration.

The cloud system extended over about 3000 km between the equator and 50° S at a longitude of around 245° W. It was observed at a solar longitude of 316°. The altitude of this system of clouds is estimated to be 92^{+30}_{-16} km. The overall characteristics rule out dust and auroral assumptions and favour clouds composed of ice crystals with effective radius in the 1–2 μm range. Two ice compositions are deemed possible for this cloud: a large-grained water ice cloud system and an extended mid-summer dawn CO_2 cloud system.

The arguments in favour of a large-grained water ice cloud system are that water ice clouds, notably at high altitudes reaching 90–100 km, have been observed during this season (dust storm season). Moreover, large-grained water ice clouds of this size are known to go higher during major storm events, and such

an event was observed at the same time as the cloud. However, there are arguments against this system. To date, water ice clouds with $1-2$ μm particle size have only been reported up to 70 km, even during global dust storms, and typical water ice clouds at 90 km are significantly smaller-grained ($0.1-0.5$ μm range).

The assumption of an extended mid-summer dawn CO_2 cloud system is fully compatible with the retrieved particle size and the altitude, typical of CO_2 ice clouds. Still, previous reports of CO_2 clouds at this L_S or at this longitude (245° E) are extremely sparse, while the observed cloud system is huge, extending beyond the equatorial latitudes down to 50° S and lasting over several hours. Differences may be related to local time as most previous report of CO_2 clouds have been obtained during daytime hours.

From our analysis, we conclude that this detached layer is an atypical ice cloud system. Extended cloud structures larger than 1000 km are indeed considered atypical, such as in Hernández-Bernal et al. (2021b), where a cloud of 1800 km is reported at 45 km altitude over Arsia Mons. The current observation is unique for its size of several thousands of kilometres, and for the combination of its particle size, altitude, and season. Future climate modelling studies may help to understand which composition, CO_2 or H_2O, is the most realistic explanation for such a cloud, and what special conditions are require for its formation.

Finally, we suggest a nucleation mechanism from cosmic rays to explain the formation of this night cloud set, which occurred on the border of a large magnetic anomaly. The role of cosmic rays has been suggested in several other planets and satellites, although not on Mars to date. Such a nucleation process may act concurrently with the above-mentioned dust storm, which protrudes dust at higher altitudes. However, the scarcity of observations prevents us from carrying out further investigations on this assumption.

References

Andrews, D., Barabash, S., Edberg, N., et al. 2016, J. Geophys. Res. Space Phys., 121, 3139

Bell, J. F., Wolff, M. J., James, P. B., et al. 1997, J. Geophys. Res., 102, 9109

Bell, J. F., I., Morris, R. V., Farrand, W. H., & Wolff, M. J. 2001, Lunar Planet. Sci. Conf., 1484

Bertaux, J.-L., Fonteyn, D., Korablev, O., et al. 2000, Planet. Space Sci., 48, 1303

Bertaux, J.-L., Leblanc, F., Witasse, O., et al. 2005, Nature, 435, 790

Branigan, T. L. 1965, Phys. Teach., 3, 303

Clancy, R. T., Wolff, M. J., Whitney, B. A., Cantor, B. A., & Smith, M. D. 2007, J. Geophys. Res. Planets, 112, E04004

Clancy, R. T., Wolff, M. J., Smith, M. D., et al. 2019, Icarus, 328, 246

Connerney, J. E. P., Acuña, M. H., Ness, N. F., et al. 2005, Proc. Natl. Acad. Sci., 102, 14970

Connour, K., Schneider, N. M., Milby, Z., et al. 2020, Geophys. Res. Lett., 47, e84997

Curtius, J., Lovejoy, E. R., & Froyd, K. D. 2006, Space Sci. Rev., 125, 159

Deighan, J., Jain, S. K., Chaffin, M. S., et al. 2018, Nat. Astron., 2, 802

Dubinin, E., Fraenz, M., Woch, J., Barabash, S., & Lundin, R. 2009, Geophys. Res. Lett., 36, L08108

Erard, S. 2000, Planet. Space Sci., 48, 1271

Forget, F., Hourdin, F., Fournier, R., et al. 1999, J. Geophys. Res., 104, 24155

Gronoff, G., Lilensten, J., Desorgher, L., & Flückiger, E. 2009a, A&A, 506, 955

Gronoff, G., Lilensten, J., & Modolo, R. 2009b, A&A, 506, 965

Haberle, R. M., Clancy, R. T., Forget, F., Smith, M. D., & Zurek, R. W. 2017, The Atmosphere and Climate of Mars (Berlin: Springer)

Haider, S. A., & Masoom, J. 2019, J. Geophys. Res. Space Phys., 124, 9566

Heavens, N. G., Johnson, M. S., Abdou, W. A., et al. 2014, J. Geophys. Res. Planets, 119, 1748

Hernández-Bernal, J., Sánchez-Lavega, A., del Río-Gaztelurrutia, T., et al. 2019, Geophys. Res. Lett., 46, 10330

Hernandez-Bernal, J., Sanchez-Lavega, A., del Rio-Gaztelurrutia, T., et al. 2021a, Geophys. Res. Lett., 48, e92188

Hernández-Bernal, J., Sánchez-Lavega, A., del Río-Gaztelurrutia, T., et al. 2021b, J. Geophys. Res. Planets, 126, e06517

Imanaka, H., Khare, B. N., Elsila, J. E., et al. 2004, Icarus, 168, 344

Jaquin, F., Gierasch, P., & Kahn, R. 1986, Icarus, 68, 442

Jiang, F. Y., Yelle, R. V., Jain, S. K., et al. 2019, Geophys. Res. Lett., 46, 7962

Jolitz, R. D., Dong, C. F., Lee, C. O., et al. 2017, J. Geophys. Res. Space Phys., 122, 5653

Kass, D. M., Kleinböhl, A., McCleese, D. J., Schofield, J. T., & Smith, M. D. 2016, Geophys. Res. Lett., 43, 6111

Kerr, R. A. 2012, Science, 336, 1498

Lavvas, P., Yelle, R. V., Koskinen, T., et al. 2012, AGU Fall Meeting Abs., 2012, P24C–04

Leblanc, F., Martinez, A., Chaufray, J. Y., et al. 2018, Geophys. Res. Lett., 45, 4685

Lilensten, J., Bernard, D., Barthélémy, M., et al. 2015, in Planetary and Space Science, 115, 48

Listowski, C., Määttänen, A., Montmessin, F., Spiga, A., & Lefèvre, F. 2014, Icarus, 237, 239

Liu, K., Hao, X., Li, Y., et al. 2020, Earth Planet. Phys., 4, 384

Määttänen, A., Montmessin, F., Gondet, B., et al. 2010, Icarus, 209, 452

Mallama, A. 2007, Icarus, 192, 404

Maret, S., Bergin, E. A., & Lada, C. J. 2006, Nature, 442, 425

McCord, T. B., Elias, J. H., & Westphal, J. A. 1971, Icarus, 14, 245

Metcalfe, L., Aberasturi, M., Alonso, E., et al. 2018, Space Sci. Rev., 214, 78

Millour, E., Forget, F., Spiga, A., et al. 2019, LPI Contrib., 2089, 6171

Molina-Cuberos, G. J., Cardnell, S., García-Collado, A. J., Witasse, O., & López-Moreno, J. J. 2018, Planet. Space Sci., 153, 157

Montmessin, F., Bertaux, J.-L., Quémerais, E., et al. 2006a, Icarus, 183, 403

Montmessin, F., Quémerais, E., Bertaux, J. L., et al. 2006b, J. Geophys. Res. Planets, 111, E09S09

Montmessin, F., Gondet, B., Bibring, J. P., et al. 2007, J. Geophys. Res. Planets, 112, E11S90

Nordheim, T. A., Dartnell, L. R., Desorgher, L., Coates, A. J., & Jones, G. H. 2015, Icarus, 245, 80

Parker, D. C., Beish, J. D., Troiani, D. M., Joyce, D. P., & Hernandez, C. E. 1999, Icarus, 138, 3

Pellier, C., Delcroix, M., Monachino, G., et al. 2020, Planetary Astronomy (USA: Axilone Astronomy)

Pomoell, J., & Poedts, S. 2018, J. Space Weather Space Clim., 8, A35

Ritter, B., Gérard, J.-C., Hubert, B., Rodriguez, L., & Montmessin, F. 2018, Geophys. Res. Lett., 45, 612

Sánchez-Lavega, A., García Muñoz, A., García-Melendo, E., et al. 2015, Nature, 518, 525

Sánchez-Lavega, A., Chen-Chen, H., Ordoñez-Etxeberria, I., et al. 2018, Icarus, 299, 194

Saunders, R. S., Arvidson, R. E., Badhwar, G. D., et al. 2004, Space Sci. Rev., 110, 1

Schmidt, R. 2003, Acta Astron., 52, 197

Schmude, Richard W., J. 1992, J. R. Astron. Soc. Canada, 86, 117

Smith, M. D., Wolff, M. J., Clancy, R. T., Kleinböhl, A., & Murchie, S. L. 2013, J. Geophys. Res. Planets, 118, 321

Spiga, A., Gonzalez-Galindo, F., López-Valverde, M.-A., & Forget, F. 2012, Geophys. Res. Lett., 39, L02201

Spiga, A., Faure, J., Madeleine, J.-B., Määttänen, A., & Forget, F. 2013, J. Geophys. Res. Planets, 118, 746

Srivastava, V. K., Kumar, J., Kulshrestha, S., et al. 2015, Adv. Space Res., 56, 671

Stack, K. M., Williams, N. R., Calef, F., et al. 2020, Space Sci. Rev., 216, 127

Stcherbinine, A., Vincendon, M., Montmessin, F., et al. 2020, J. Geophys. Res. Planets, 125, e06300

Svensmark, H., & Friis-Christensen, E. 1997, J. Atm. Sol. Terres. Phys., 59, 1225

Vincendon, M., Langevin, Y., Poulet, F., Bibring, J.-P., & Gondet, B. 2007, J. Geophys. Res. Planets, 112, E08S13

Vincendon, M., Pilorget, C., Gondet, B., Murchie, S., & Bibring, J.-P. 2011, J. Geophys. Res. Planets, 116, E00J02

Zurek, R. W., & Smrekar, S. E. 2007, J. Geophys. Res. Planets, 112, E05S01

Appendix A: Estimation of the resolution

A.1. Scale in the images

In all the images, the Mars disc size is 180 pixels from pole to pole. With the planet diameter equal to 6780 km, we can deduce the scale in our images, 1 pixel corresponding to $\frac{6780}{180}$ = 37.6 km. Even so, this scale is projected in the plane of the image. Therefore, without further calculation, it can be applied to measure a feature only at the centre of the disc.

A.2. Theoretical resolution

From the Sparrow criterion, the point spread function (PSF) due to the diffraction effect is FWHM = $\frac{1.02\lambda}{D}$, where FWHM is the theoretical full width at half maximum of the PSF (in radians), λ is the observation wavelength (in metres), and D the diameter of the instrument aperture (in metres). As D = 0.356 and λ = 550 10^{-9} (green filter), the spatial resolution is 0.32". The Mars apparent size is 16.9". As mentioned above, Mars size corresponds to 180 pixels. The angular scale is therefore 0.094" pixel. The theoretical resolution is then equal to $\frac{0.32}{0.094}$ = 3.4 pixels.

From the above, we deduce that the theoretical resolution is 3.4 x 37.6 = 128km. If we use the Rayleigh criterion ($FWHM = \frac{1.22\lambda}{D}$) instead of the Sparrow criterion, we arrive at a theoretical resolution of 150 km.

A.3. Practical resolution

In order to further determine the actual resolution of our observations, we could extract the Olympus Mons caldera, which is visible as a dark spot in some images. This is one of the smallest details visible on Mars from our images (figure A.1). The RGB picture from Mars Global Surveyor (MGS) allows us to see this caldera, whose size is 80x60 km. The caldera, which cannot be resolved in a 356 mm diameter telescope, appears as a dark spot in some green filter images when approaching the evening limb; it is brighter in broad daylight.
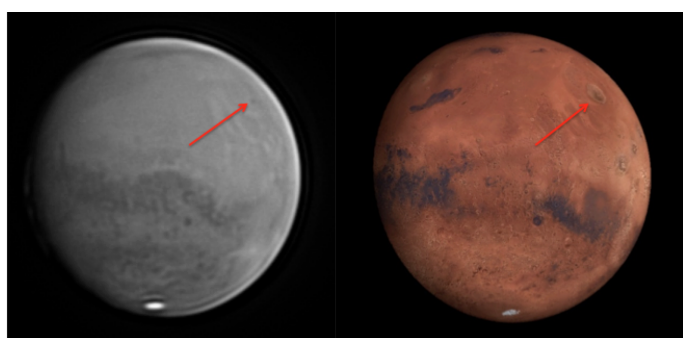

Fig. A.1. Extraction of the Olympus Mons caldera from our observations. Left panel: Green filter. Right panel: MGS natural colours. The arrow shows the location of the Mons.

In order to get the PSF of this unresolved detail, which gives the effective resolution of the images, we plot the intensity profile on a cross-section of the caldera in Figure A.2. We can determine the FWHM of the dark spot, which comes to 3.3 to 3.5 pixels. This FWHM is similar to the theoretical resolution of 3.4 pixels from the Sparrow criterion. This indicates that the practical resolution is identical to the theoretical value (i.e. 3.4 pixels, or 128 km in projection).
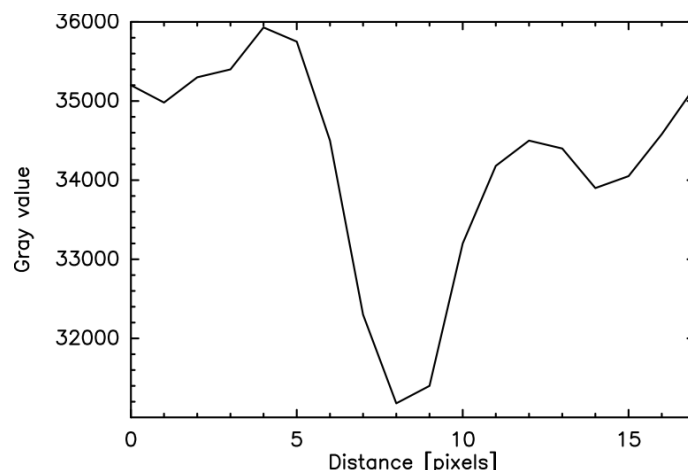

Fig. A.2. Intensity profile of a cross-section of Olympus Mons caldera

Appendix B: Solar activity conditions on Mars during the observations

Figure B.1 shows the solar wind conditions on Mars between 12 and 22 November 2020. To simulate these conditions, we used a GONG Air Force Data Assimilative Photospheric Flux Transport model (ADAPT) magnetogram on 2020-11-12T00:00 as initial input. Then we performed a forecast for a total of ten days. The results show that a fast solar wind flow impacts the planet after 19 November. The solar wind velocity increases to more than 400 km.s^{-1} preceded by an increase in density and pressure due to the compression of the upcoming fast solar wind with the preceding slow solar wind. An increase in the total magnetic field strength is also observed due to that compression. The sudden drop in the magnetic field (due to the sudden drop in the azimutal component, B$_{lon}$) indicates that Mars encountered a heliospheric current sheet (HCS) crossing.

Appendix C: Captions for Movies

C.1. Movie S1

Evolution of the cloud for 17 November in the green band, 20:25 to 21:15 UT.

C.2. Movie S2

Evolution of the cloud for 17 November in the green band, 19:58 to 22:36 UT

C.3. Movie S3

Evolution of the cloud for 17 November in the red band, 19:54 to 22:52 UT

C.4. Movie S4

Evolution of the cloud for 17 November with all features annotated in order to compute their altitudes, 20:25 to 21:42 UT. The band is indicated on each frame. G stands for green and R for red.
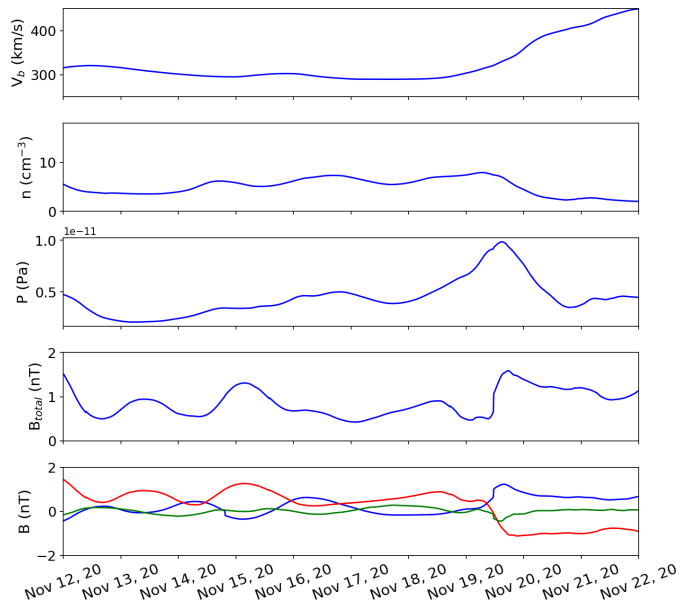
Fig. B.1. EUHFORIA simulation. From top to bottom: Solar wind plasma velocity, density, pressure, total magnetic field, and the three magnetic field components (blue: radial, red: longitudinal, green: colatitudinal in the Heliocentric Earth Equatorial, HEEQ, coordinate system), between 12 and 22 November 2020 on Mars.